Quantized liquid density-functional theory for hydrogen adsorption in nanoporous materials

Serguei Patchkovskii* and Thomas Heine†
Steacie Institute for Molecular Sciences, NRC, 100 Sussex Drive, Ottawa, Ontario, Canada K1A 0R6
and School of Engineering and Science, Jacobs University Bremen, D-29759 Bremen, Germany
(Received 13 May 2009; revised manuscript received 17 July 2009; published 16 September 2009)

We develop a finite-temperature quantized version of density-functional theory of atomic and molecular liquids (QLDFT). Following the Kohn-Sham partitioning of the free energy, we introduce a noninteracting reference fluid of particles obeying the Maxwell-Boltzmann statistics. The kinetic and potential energy of the reference fluid are evaluated exactly. All remaining contributions, including interactions between fluid particles and corrections due to the appropriate quantum statistics are subsumed by an excess (in electronic DFT called exchange-correlation) functional. Two variants to approximate the excess functional are presented: the simplest local-interaction expression (LIE-0) avoids the direct calculation of interparticle interactions and includes them in the excess functional, which is parametrized to reproduce experimental equation of state of normal hydrogen. The more sophisticated LIE-1 approximation is based on the weighted local-density approximation and includes the explicit interparticle interaction potential as well as the local approximation of the excess functional, the latter being weighted by the average over a spherical environment to include nonlocal effects in an approximate way. We apply LIE-0 and LIE-1 to two benchmark systems, bulk fluid hydrogen and hydrogen in a slit pore, and compare it with classical molecular-dynamics simulations employing the same potential. Both functionals produce similar results for direct quantum effects in adsorption free energy. At the same time, LIE-1 also yields a reasonable description of the fluid structure and classical packing effects, which are not reproduced by LIE-0. The source code of our implementation of the LIE-QLDFT is distributed under the GNU public license and is included as a supporting material.

DOI: 10.1103/PhysRevE.80.031603 PACS number(s): 68.43.De, 64.60.De, 67.10.Fj, 05.30.−d

I. INTRODUCTION

Theoretical description of adsorption of fluids in microporous media has been the subject of extensive investigations for many years (see, e.g., [1–4] and references therein). The intense interest in the field has been rekindled recently by the improvements in preparation and characterization of uniform nanoporous substrates [5–7]. Porous networks with typical channel apertures comparable to the adsorbate molecule sizes have shown remarkable potential in gas [8,9] and isotope [10,11] separation, as well as very high specific surface areas and guest molecule uptakes [12].

Potentially high adsorption capacity of nanoporous materials toward light gases is of a particular practical interest due to the ongoing efforts to contain vehicular carbon dioxide emissions. The release of CO_2 to the atmosphere from the combustion of fossil fuels is one of the largest contributions to the greenhouse effect [13]. While for stationary power production alternatives to fossil energy carriers are well-established mobile applications still rely almost exclusively on the combustion of liquid oil-based fuels such as gasoline, diesel, or kerosene. These fuels have the advantage of a very high-energy density (30 MJ/kg for octane) and can be distributed easily and reasonably safely.

A promising design for CO_2 emission-free vehicles are fuel cell-powered cars utilizing molecular hydrogen [14]. While efficient fuel cells, which electrochemically oxidize hydrogen and release electric power, are already available [15], the prototype vehicles still rely on high-pressure or low-temperature liquefied hydrogen tanks. Either solution requires sophisticated (and expensive) infrastructure for hydrogen distribution and encounters hard to overcome safety issues. Indeed, the biggest challenge for hydrogen-powered mobile applications remains the development of weight- and volume-efficient hydrogen storage system.

One of the possibilities for a compact H_2 storage device is physisorption in nanostructures, where compression of hydrogen fluid is assisted by attractive guest-host interactions. Several nanostructures have been explored as potential H_2 storage devices, including graphene slit pores, carbon nanotubes (for a critical review see [16]), and metal-organic frameworks [5]. The capability for prediction and analysis of the storage capacity of such structures is clearly important. This is obviously the case where hypothetical nanostructures are suggested to experiment. Additionally, the experimental challenges inherent in hydrogen adsorption work [17] and especially in activated carbon samples [6,8,18] make it desirable to provide a backup consistency check for experimental measurements.

Currently, the "standard" theoretical treatment of hydrogen adsorption in nanostructures is through grand-canonical Monte Carlo (GCMC) simulations [19]. Due to the low molecular weight of the H_2 guest—the lightest known stable species—quantum effects may also become important even at relatively high temperatures [11,20,21]. Quantum contributions are typically approached though path-integral GCMC (PI-GCMC) simulations [22] or closely related high-temperature approximations [11,21,23]. Although in principle exact for any given interaction potential, GCMC and especially PI-GCMC simulations are computationally and labor intensive.

*serguei.patchkovskii@nrc.ca
†t.heine@jacobs-university.de

The well-known and economical alternative to GCMC fluid simulations is offered by the density-functional theory of classical liquids (CLDFT) [24–26]. (See, e.g., [1,3,27–29] for a recent overview.) CLDFT and the closely related field theories [30–32] have been manifestly successful in modeling structure and thermodynamics of bulk fluids, phase transitions (see [4] for a review) and nucleation (see [33] for a review), phase mixing [8,34,35], fluid-solid interfaces [36–38], capillary phenomena (see [2] for a review), colloidal solutions [39,40], and adsorption in microporous solids [41,42]. Efficient large-scale CLDFT calculations of arbitrary three-dimensional (3D) geometries are possible [43]. Provided that modern nonlocal excess free-energy functionals [28,44–46] are used, CLDFT predictions agree quantitatively with experimental results for adsorption of heavy supercritical fluids [7,8,42,47]. Incorporation of quantum effects in the liquid density-functional theory (LDFT) treatment appears to be needed for achieving similar-quality results for nanosorbed light molecular fluids.

The formal exact DFT treatment of quantum liquids has been known for some time [48,49]. Most of the practical applications have centered on low-temperature liquids, where either the quantum degeneracy limit (Bose or Fermi condensate limit) [50–56] or gradient expansion for slowly varying densities [57] are particularly useful for approximating the kinetic-energy functional. The notable exceptions are a path-integral extension of LDFT [58,59] and quantization corrections due to fluid cell effect [60,61]. The finite-temperature treatment of Biben and Frenkel [62] is in the same spirit as our work but has been implemented only for fluid helium and would be challenging to apply at higher temperatures where many states become populated.

Here, we explore an alternative approach toward construction of a practical quantized liquid density-functional theory (QLDFT). Following the Kohn-Sham partitioning of the free-energy [48] standard in electronic DFT, we introduce the noninteracting "reference" fluid. The canonical-ensemble free energy of the reference fluid is evaluated exactly [63] and efficiently [64]. The remaining contributions due to particle correlations are incorporated in the excess (XC) functional (in electronic DFT called exchange-correlation functional), parametrized to reproduce the experimental equation of state of fluid hydrogen.

In the remainder of this paper, we outline the canonical-ensemble Kohn-Sham formulation of quantized liquid density-functional theory (Sec. II) and two approximations to the excess functional: the simplest local-interaction expression (LIE-0) form of the excess free-energy functional which includes the interparticle interaction potential in the excess functional; and the more sophisticated LIE-1 form, which includes the explicit interparticle potential and applies the Moroni-Senatore form of weighted density approximation (WDA) [25,65,66] (Sec. II D), to account for (a fraction of) nonlocal effects. We briefly describe an efficient linear-scaling computational implementation of the resulting self-consistent integrodifferential equations (Sec. III). The method and implementation is tested for two well-known benchmark systems: fluid hydrogen in free space and within a slit pore (Sec. IV). Where appropriate, results are compared to classical molecular-dynamics (MD) simulations. The magnitude of quantum effects in LIE-QLDFT is discussed in Sec. IV C. Conclusions and outlook for possible future developments are collected in Sec. VI.

Finally, Appendix B gives explicit expressions for the LIE-0 and LIE-1 XC functionals, while the complete source code of our QLDFT implementation, provided under the terms of the GNU general public license [67], is included as a supplementary material [68].

II. QUANTIZED DENSITY-FUNCTIONAL THEORY OF FLUIDS

Density-functional theory of fluids is customarily developed within the grand canonical μVT ensemble [48,49,62], with the volume of the system V, temperature T, and chemical potential μ held constant. For reasons outlined below, we choose instead to work with the canonical NVT ensemble (sometimes also used in CLDFT, although less often [2]), constraining the number of particles N. In the thermodynamic limit both ensembles should lead to identical results although significant differences do arise for small particle counts (see, for example, [69]). Because the derivation is essentially identical to the well-known treatment in electronic DFT [48], we will only show the key expressions necessary to establish the notation.

A. QLDFT model

Following the Kohn-Sham partitioning [48] of the free-energy functional, we introduce a fictitious noninteracting reference fluid of particles obeying Boltzmann statistics [58,59]. (The discussion and justification of this and other assumptions and approximations are relegated to the end of this section.) The corresponding noninteracting one-particle density matrix $\rho_S(r,r')$ is given by the standard expression [70]:

$$\rho_S(\mathbf{r},\mathbf{r}') = \mathcal{Z}_S^{-1} \exp(-\beta \hat{H}_S), \tag{1}$$

where β is the inverse temperature [$\beta=(k_BT)^{-1}$, with k_B being the Boltzmann constant]. The canonical noninteracting one-particle partition function $\mathcal{Z}_S$ is given by

$$\mathcal{Z}_S = \mathrm{Tr} \exp(-\beta \hat{H}_S), \tag{2}$$

where Tr is the trace operator.

The density matrix ρ is determined by an auxiliary noninteracting effective Hamiltonian $\hat{H}_S$ given by a sum of the kinetic-energy operator, the mean-field potential, and the multiplicative potential v_{eff}:

$$\hat{H}_S = -\frac{\hbar^2}{2m}\Delta + v_{\mathrm{eff}}(\mathbf{r}), \tag{3}$$

$$v_{\mathrm{eff}}(\mathbf{r}) = v_{\mathrm{ext}}(\mathbf{r}) + \int v_{12}(\mathbf{r}-\mathbf{r}')n(\mathbf{r}')d\mathbf{r}' + v_{\mathrm{XC}}(\mathbf{r}), \tag{4}$$

where v_{ext} is the external potential, and integration is over the entire volume of the system. In Eq. (4), $n(\mathbf{r})$ is the particle density for the real interacting system. The two-body

interaction potential between particles of the fluid is given by v_{12}. The excess potential v_{XC} is a functional of the physical density $n(\mathbf{r})$. It is chosen such that after normalization to the number of particles, the diagonal of the noninteracting density matrix coincides with the physical density:

$$n(\mathbf{r}) = N\rho_S(\mathbf{r},\mathbf{r}). \tag{5}$$

The free-energy functional $F_{tot}[n] \equiv F_{tot}[\rho_S]$ of the interacting fluid can now be written as [48]

$$F_{tot}[\rho_S] = F_S[\rho_S] - \frac{1}{2}\int n(\mathbf{r})v_{12}(\mathbf{r}-\mathbf{r}')n(\mathbf{r}')d\mathbf{r}d\mathbf{r}' - \int v_{XC}(\mathbf{r})n(\mathbf{r})d\mathbf{r} + F_{XC}[n], \tag{6}$$

$$F_S[\rho_S] = -\frac{N}{\beta}\ln\frac{\mathcal{Z}_S}{N}, \tag{7}$$

where F_S is the free-energy functional for the ideal noninteracting system in the external potential given by v_{eff}. The F_S contribution contains the kinetic energy of the noninteracting reference fluid and the potential energy of the real fluid in the external field. The second term in Eq. (6) corrects for double counting of the mean-field interaction energy in Eq. (7), while the third term cancels the contribution of the excess potential v_{XC} in Eq. (4) to F_S. Finally, the functional F_{XC} incorporates all remaining contributions to the free energy of the real gas. It includes the difference between noninteracting and real kinetic energy, correction factors due to the difference in particle statistics of the reference and interacting fluids, as well as the difference between the mean-field ideal and real interparticle interaction energies. The universal functional F_{XC} is in general unknown but is assumed to exist for any reasonable choice of interparticle interaction potential v_{12} [71].

The minimum of the functional $F[\rho_S]$ for a given external potential $v_{ext}(r)$ gives the equilibrium free energy of the system [72]. The corresponding particle density n_{eq} gives the equilibrium density distribution. By construction, Eq. (5) imposes the restriction on the total number of particles in the system for any choice of the auxiliary density matrix ρ. Then, unconstrained variational minimization [73] of Eq. (6) with respect to ρ establishes the relationship between the functionals F_{XC} and v_{XC}:

$$v_{XC}(r) = \frac{\delta F_{XC}[n]}{\delta n(\mathbf{r})}. \tag{8}$$

B. Assumptions and approximation of the model

We are now in a position to discuss the assumptions and approximations inherent in Eqs. (1)–(8). In principle, the noninteracting reference system in Eqs. (1) and (2) should obey the quantum statistics (Bose-Einstein or Fermi-Dirac) appropriate for the total spin of the fluid particles [74]. At the same time, for bosonic H_2 the deviations from Boltzmann statistics only become noticeable at temperatures well below those of interest for hydrogen adsorption [58,59,75]. If degeneracy effects were to become important, the appropriate statistics could be included by the standard modification [70] of the ideal-gas expressions in Eqs. (1), (2), (5), and (7).

The interaction potential [v_{12} in Eq. (4)] must be a function of the interparticle separation alone and cannot depend on the external potential or on hidden internal state of the particles. This condition arises from the separability of the external potential and the interparticle contributions to the Hamiltonian, which is required for the proof of the Hohenberg-Kohn theorem [48]. The relevant internal state (given by the orientation of the permanent or induced multipole moments, bond lengths and angles, etc.), if present, must be explicitly included in the variational minimization of F_{tot}. Internal degrees of freedom, in particular relative orientations between individual particles, are averaged out in this treatment, a good approximation for temperatures at 77 K and higher. A more rigorous treatment of the internal degrees of freedom more evaporate but straightforward and will be discussed elsewhere [76].

The interaction potential v_{12} is taken to be in a pairwise additive form. In principle, three- or many-body potentials could be accommodated by including higher-order mean-field integrals in Eq. (4) and the compensating terms in Eq. (6) (however, see [27] for a discussion of possible pitfalls of taking this approach). Since the microscopic Hamiltonian for the interacting system of nuclei and electrons does not contain higher than two-body terms, the appearance of high-order terms in Eq. (4) would suggest the presence of an essential hidden state for the fluid particles. Incorporation of the corresponding internal parameters (such as the orientational preference, electric polarization, or structural deformation) in the state vector should then recover the desired simple pairwise form of the interaction potential.

The noninteracting density matrix in Eq. (1) is defined within the canonical ensemble. At the same time, the form of the physical density n in Eq. (5) is compatible with noninteger particle counts N. Such fractionally populated ensembles should be interpreted [77] as a linear interpolation between systems with $[N]$ and $[N]+1$ particles. In particular, fractionally populated ensembles in the form of Eq. (5) do not imply fluctuations in the particle count, whose description would require a grand-canonical ensemble. In principle, fluctuations can be recovered by a field theory constructed from the present canonical QLDFT, similar to the situation encountered for classical fluids [31,78]. Let us finally note that the exact canonical excess free-energy functional should undergo a derivative discontinuity at integer occupation numbers [77] (also see [79,80] for the analysis of a closely related issue in canonical classical DFT).

C. Local-interaction expression or local-density approximation (LIE-0)

Practical QLDFT calculations require an explicit form for the interparticle interaction potential v_{12} and the free-energy functional F_{XC}. The simplest possible form for $F_{XC}[n]$ is the local-density approximation (LDA):

$$F_{\mathrm{XC}}[n] = \int n(\mathbf{r})\varepsilon_{\mathrm{XC}}[n(\mathbf{r})]d\mathbf{r}, \tag{9}$$

where the excess energy density $\varepsilon_{\mathrm{XC}}$ is a local function of the particle density, and integration is over the entire space. The matching excess potential is given by [73]

$$v_{\mathrm{XC}}(\mathbf{r}) = \varepsilon_{\mathrm{XC}}[n(\mathbf{r})] + n(\mathbf{r})\frac{\partial \varepsilon_{\mathrm{XC}}}{\partial n}. \tag{10}$$

For a *uniform* fluid with volume V, average density n_{av}, and total number of particles $N=n_{av}V$, substitution of Eqs. (9) and (10) into Eq. (6) gives the per-particle free energy of

$$\frac{F(N,V)}{N} = -\frac{1}{\beta}\ln\frac{Z_S}{n_{av}V} - \frac{n_{av}}{2}\int v_{12}(\mathbf{r})d\mathbf{r} - n_{av}\frac{\partial \varepsilon_{\mathrm{XC}}}{\partial n_{av}}. \tag{11}$$

If the external potential in Eq. (4) vanishes, the kinetic- and potential-energy contributions to the noninteracting effective Hamiltonian commute. Explicit evaluation of the v_{eff} contribution to the partition function then gives

$$\frac{F(N,V)}{N} = -\frac{1}{\beta}\ln\frac{Z_{kin}}{n_{av}V} + \frac{n_{av}}{2}\int v_{12}(\mathbf{r})d\mathbf{r} + \varepsilon_{\mathrm{XC}}(n_{av}). \tag{12}$$

In principle, the kinetic partition function Z_{kin} [Eq. (2) evaluated with $v_{eff}\equiv 0$] could be replaced by its high-temperature limit [74],

$$Z_{kin} = V\left(\frac{m}{2\pi\beta}\right)^{3/2}, \tag{13}$$

or by the similar exact limit for the cyclic Hamiltonian (Appendix A). At the same time, a significant computational advantage can be realized by incorporating a counterpoise [81] correction in Z_{kin}, as described below (Sec. III).

If the per-particle free energy $\mathcal{F}(n)=\frac{F(N,V)}{N}$ of the uniform fluid of density n is available from experiment or from a higher-level calculation, Eq. (12) leads to an explicit expression for the LDA excess free-energy density:

$$\varepsilon_{\mathrm{XC}}(n) = \mathcal{F}(n) + \frac{1}{\beta}\ln\frac{Z_{kin}}{nV} - \frac{n}{2}\int v_{12}(\mathbf{r})d\mathbf{r}. \tag{14}$$

From Eq. (14), it is clear that the choice of the mean-field interaction potential v_{12} in the LDA version of QLDFT is not unique: any integrable $v_{12}(r)$ will leave the uniform gas results unchanged. The potential v_{12} must therefore be chosen on other grounds. In the LDFT treatment of classical fluids, it is customary to separate a given interparticle interaction potential into a short-range purely repulsive term, and a longer-range attractive contribution [39]. The repulsive potential is treated through a local or quasilocal excess functional, while the long-range tail becomes the mean-field potential v_{12}.

For hydrogen storage problems, the high-density regime at temperatures well above the critical point is of primary interest. Interparticle interactions in this limit are predominantly repulsive and are often adequately described by the LDA. The attractive tail of the potential is particularly shallow for hydrogen (<55 K [82]) and has only minimal influence on the structure of high-density fluids [83]. It therefore appears justified to set the mean-field contribution to zero:

$$v_{12}(\mathbf{r}) \equiv 0, \tag{15}$$

and to represent the intrinsic properties of the fluid through the excess free-energy density $\varepsilon_{\mathrm{XC}}$ alone. Note that this choice does not amount to the complete neglect of attractive hydrogen-hydrogen interactions. These contributions are still included in $\varepsilon_{\mathrm{XC}}$, albeit in a more approximate way.

To clearly distinguish this approximation from the more rigorous and accurate LDA treatment with $v_{12}\neq 0$, we will refer to the $v_{12}\equiv 0$ case as a "*local interaction expression*" (LIE-0).

It remains to determine the numerical expression for the excess functional. We extract the uniform-fluid molar free energy $\mathcal{F}$ from the experimental data of Mills *et al.* [84], who determined the p-V-T diagram and sound velocity of fluid n-H_2 in the range $75<T<307$ K and $2<p<20$ kbar. The resulting data set is fit to an equation of state of Benedict type. Standard thermodynamic integration leads to explicit expressions (given in Appendix B) for $\mathcal{F}(p,T)$. Extrapolation of the resulting $\mathcal{F}$ to lower pressures shows an acceptable agreement with low-pressure experimental data ($p<2$ kbar [85]).

It should be pointed out that our choice of the excess functional is not entirely consistent with the use of the canonical ensemble. The experimentally derived $\mathcal{F}$ is defined for a macroscopic system and thus corresponds to a constant chemical potential (the grand-canonical ensemble). In principle, it would have been possible to correct the resulting functional for finite-size effects. The differences between grand-canonical and canonical excess functionals primarily manifest themselves in the fluid structure [86,87] rather than in the integrated properties. Our choice of the mean-field interaction v_{12} already precludes a detailed description of the density oscillations. As a result, we have decided against applying the canonical correction.

The approximate LIE-0 form of QLDFT outlined above becomes exact in two important limits [48]:

(i) In the limit of low density, where interparticle interactions are negligible, LIE-0 QLDFT reduces to the ideal-gas adsorption equation for the quantized Boltzmann gas. As a result, an accurate description may be expected for the initial rising slope of the adsorption isotherms.

(ii) In the limit of slowly varying potential (or high particle density, where the mean free path of the particles becomes much shorter than the characteristic size of the external potential), LIE-0 reduces to hydrostatic equations. Unlike the scaled ideal-gas approximation [63,64], a small gradient of the external potential is sufficient to achieve the hydrostatic limit; no restriction is imposed on the overall variation in the potential.

The existence of the physically well-motivated exact limits suggests that LIE-0 QLDFT may turn out to be a useful description of nanosorbed supercritical fluids at the intermediate densities as well. However, given the number and extent of approximations, the reliability of the theory should

ultimately be judged from its performance in practical calculations.

D. Local-interaction expression with explicit interparticle interactions and weighted local-density approximation (LIE-1)

The explicit hydrogen-hydrogen interaction potential v_{12} could be incorporated into the LDA effective Hamiltonian in a straightforward way [Eq. (14)]. However, the short-range repulsive part of this interaction introduces a rapidly oscillating potential and consequently strongly oscillating density leading to severe numerical problems for a purely local functional and finite grid spacings. The situation is not dissimilar to numerical imbalance between wave function and electron density representations in electronic structure calculations but is exacerbated by the strong correlations induced by the hard-core part of the v_{12} potential in molecular fluids. The standard solution to the problem is through the weighted local-density approximation (WLDA) [25,65,66]. Here, the excess energy functional depends not only on the local particle density, but also on the average density in the vicinity [the weighted density $\bar{n}(\mathbf{r})$], which is constructed by applying convolution filter $w(|\mathbf{r}'-\mathbf{r}|)$ to the particle density around probe position $\mathbf{r}$:

$$\varepsilon_{\mathrm{XC}} = \varepsilon_{\mathrm{XC}}[n(\mathbf{r}),\bar{n}(\mathbf{r})], \tag{16}$$

$$\bar{n}(\mathbf{r}) = \int w(|\mathbf{r}'-\mathbf{r}|)n(\mathbf{r}')d\mathbf{r}'. \tag{17}$$

The WLDA excess functional is then given in the usual form

$$F_{\mathrm{XC}}[n] = \int n(\mathbf{r})\varepsilon_{\mathrm{XC}}[n(\mathbf{r}),\bar{n}(\mathbf{r})]d\mathbf{r}. \tag{18}$$

The weighted density yields additional terms in the excess potential [66]:

$$v_{\mathrm{XC}} = \frac{\delta F_{\mathrm{XC}}}{\delta n} = \varepsilon_{\mathrm{XC}}[n(\mathbf{r}),\bar{n}(\mathbf{r}')] + n(\mathbf{r})\frac{\partial \varepsilon_{\mathrm{XC}}}{\partial n}[n(\mathbf{r}),\bar{n}(\mathbf{r})] + \int n(\mathbf{r}')\frac{\partial \varepsilon_{\mathrm{XC}}}{\partial \bar{n}}[n(\mathbf{r}),\bar{n}(\mathbf{r}')]w(|\mathbf{r}-\mathbf{r}'|)d\mathbf{r}'. \tag{19}$$

The connection to the uniform gas solution now gives [cf. Eq. (14)]

$$\varepsilon_{\mathrm{XC}}(n,\bar{n}) = \mathcal{F}(\bar{n}) + \frac{1}{\beta}\ln\frac{\mathcal{Z}_{kin}}{\bar{n}V} - \frac{n}{2}\int v_{12}(\mathbf{r})d\mathbf{r}. \tag{20}$$

Note that in Eq. (20) we have chosen to treat the experimental molar free energy $\mathcal{F}$ as a function of the weighted density *alone*. Other choices are possible as well [88] but would require more experimental data to fix the explicit form of $\mathcal{F}$. Furthermore, we have chosen to make the statistical factor in the noninteracting kinetic-energy term to be a function of the weighted density $\bar{n}$ rather than the local density n. The latter choice is needed to ensure that structures in density profiles become less pronounced with increasing temperature. Using the local density n in the $1/\beta \ln \mathcal{Z}_{kin}/\bar{n}V$ term leads to an unphysical *increase* in the magnitude of density oscillations with temperature.

The two derivatives of $\varepsilon_{\mathrm{XC}}$ with respect to the true and the weighted densities are

$$\frac{\partial \varepsilon_{\mathrm{XC}}}{\partial n} = -\frac{1}{2}\int v_{12}(\mathbf{r})d\mathbf{r}, \tag{21}$$

$$\frac{\partial \varepsilon_{\mathrm{XC}}}{\partial \bar{n}} = \frac{\partial \mathcal{F}(\bar{n})}{\partial \bar{n}} - \frac{1}{\beta \bar{n}}. \tag{22}$$

Two components of the LIE-1 functional has so far been left unspecified: the interparticle potential $v_{12}(\mathbf{r})$ and the convolution filter $w(r)$. The selection we make should be appropriate for the problem of hydrogen storage at reasonably high temperatures. Diep and Johnson studied the H_2-H_2 interactions in detail and expanded the interparticle potential in a series of spherical harmonics [82]. We assume that at 77 K and above all relative orientations of the H_2 molecules are equally probable and therefore take only the leading, isotropic term of this series, which depends only on the interparticle distance. (Our choice remains valid as long as the local anisotropies in the H_2-H_2 and external potentials are small compared to $4B_e \approx 340$ K, where B_e is the H_2 rotational constant.) In order to maintain variational stability of the functional, the integral $\int v_{12}(\mathbf{r})d\mathbf{r}$ must not become negative. We satisfy this condition by replacing the short-range part of v_{12} with an arc segment, matching the slope of the initial $v_{12}(\mathbf{r})$ at the zero crossing point. The maximum of the arc segment, reached at $r=0$, is $v_{max}=+180$ K. The $w(r)$ convolution filter operates in the same region and is designed to vanish close to the zero crossing point. We have chosen the normalized Fermi-Dirac function:

$$w(r) = \left\{8\pi d^3 \mathrm{Li}_3\left[-\exp\left(\frac{r_0}{d}\right)\right]\left[1+\exp\left(\frac{r-r_0}{d}\right)\right]\right\}^{-1}, \tag{23}$$

where Li_3 is the third order polylogarithmic function, and parameters r_0 and d are set, respectively, to 2.500 and 0.001 Å. The numerical values of v_{max}, r_0, and d have been determined by fitting the parameters to density profiles obtained by classical molecular-dynamics simulations of H_2 adsorbed in a hard-wall slit pore (see below).

III. COMPUTATIONAL IMPLEMENTATION AND TECHNICAL DETAILS

We solve the LIE-QLDFT equations numerically, on a three-dimensional uniform Cartesian-space product grid. We employ periodic boundary conditions in the Γ-point approximation. The Laplacian operator [Eq. (3)] is discretized using the standard three-point expression. Sparsity of the Hamiltonian and the density matrices is used to achieve $O(N)$ computational scaling with the number of grid points. By casting all expressions in terms of density matrices, we avoid the need to explicitly construct the noninteracting reference wave function. Although useful at low temperatures and in

reduced-dimensionality systems, where only a small number of levels are significantly populated [62], explicit diagonalization of the effective Hamiltonian has an extremely unfavorable scaling for large systems and at higher temperatures [64]. Further technical details, accuracy control and convergence of the numerical techniques are similar to the quantized ideal-gas treatment reported previously [64] and need not be repeated.

Numerical implementation of the LIE-1 functional requires evaluation of several convolutions at grid points, namely, the mean-field potential [second term in Eq. (4)], the weighted density $\bar{n}$ [Eq. (17)], and the nonlocal contribution to the excess potential [the final term in Eq. (19)]. The required integrals are implemented with Fourier transforms and give a negligible contribution to the total computational cost.

Due to the mutual dependence of the density n and the excess potential v_{XC}, the self-consistent solutions of QLDFT equations are obtained by damped stationary-point iterations starting from a suitable starting guess [62]. Once the external potential is determined, the solution proceeds as follows:

(1) Guess the initial particle density $n(\mathbf{r})$. The possibilities include:

(i) $n=0$. The initial iteration employs the ideal gas approximation [64]. The ideal-gas starting guess often leads to convergence problems at low temperatures and high densities and would normally be used only to bootstrap the evaluation of an adsorption isotherm.

(ii) Densities obtained as solution of CLDFT equations. Calculations starting with the classical guess tend to converge rapidly at higher temperatures ($T>150$ K) and moderate densities.

(iii) Renormalized converged QLDFT densities obtained at similar temperatures and particle counts. Renormalized densities may be needed to achieve convergence at lower temperatures ($T<150$ K) and particle densities approaching density of solid hydrogen.

(2) For the initial iteration, set n_1 to n, and proceed to the next step. Otherwise, construct the damped density guess (n_i) for the next iteration by mixing the guess density of the previous iteration (n_{i-1}) with the final density of the previous SCF cycle (n):

$$n_i(\mathbf{r}) = \alpha_n n(\mathbf{r}) + (1-\alpha_n) n_{i-1}(\mathbf{r}). \tag{24}$$

(3) Evaluate the excess potential v_{XC} using Eqs. (10) and (14) and the current guess for the particle density n_i.

(4) For the initial iteration, set $v_{\mathrm{XC},1}=v_{\mathrm{XC}}$, and proceed to the next step. Otherwise, construct the new damped guess for the excess potential:

$$v_{\mathrm{XC},i}(\mathbf{r}) = \alpha_v v_{\mathrm{XC}}(\mathbf{r}) + (1-\alpha_v) v_{\mathrm{XC},i-1}(\mathbf{r}). \tag{25}$$

(5) Determine the effective potential v_{eff} [Eq. (4)] and calculate the one-particle density matrix of the noninteracting reference system [Eqs. (1) and (2)] using the series expansion of matrix exponentiation operator, as described elsewhere [64].

(6) Obtain the new particle density n by renormalizing the diagonal of the noninteracting density matrix ρ_S [Eq. (5).

(7) Calculate the post-SCF contributions and the total QLDFT free energy from Eq. (6).

(8) Convergence test: if the maximum absolute change in particle densities n_i and n_{i-1} is less than ε_n, and the absolute change in the free energy from the previous iteration does not exceed ε_F, QLDFT iterations have converged. Otherwise, return to step III. Typical values of the convergence criteria are $\varepsilon_F=0.1$ J mol^{-1} and $\varepsilon_n=10^{-3}$ Å^{-3}.

Two aspects of this iterative procedure deserve a separate discussion. Because of the highly nonlinear dependence of the effective potential on the guess density, undamped iterations of the algorithm ($\alpha_n=\alpha_v=1$) typically diverge. In the three-dimensional classical-fluid DFT calculations, it is common to replace the stationary-point procedure with a second-order direct minimization of the free energy [43]. The direct minimization approach requires first and (possibly an estimate of) second derivatives of the total free energy [Eq. (6)] with respect to particle density $n(\mathbf{r})$. In QLDFT, it would have been necessary to evaluate the derivatives of the corresponding exponential operator [Eq. (2) and (7)]. As the effective potential and kinetic energy terms in the Hamiltonian of Eq. (3) do not commute, the effort is nontrivial [89,90]. Instead, we find that the simple double mixing procedure with $\alpha_n=\alpha_F\approx 0.1$ typically converges although stronger damping may be needed at high densities and extreme confinement geometries. Both density and effective potential mixing are essential for reducing the oscillations in the SCF cycles. The effective-potential mixing prevents the excessive "flow" of the particle density between spatial regions where large differences in the external potential are counteracted by relatively small changes in the density of highly compressed fluid. The density mixing reduces "sloshing" within regions of slowly varying adsorption potential, where the potential mixing is less efficient.

The second important refinement of the computational procedure is the built-in grid counterpoise correction [81]. The evaluation of the excess energy density [Eq. (14)] and the excess potential [Eq. (10)] requires the one-particle partition function in the free space (Z_{kin}). If the analytical limit is used for Z_{kin} [either Eq. (13) or the more elaborate Eq. (A6)], very dense numerical grids are needed to approach useful convergence for the adsorption free energy. The same results can be obtained with less effort if Z_{kin} is taken from Eq. (A3), evaluated on the grid used for the adsorption calculation. All results reported below were obtained using the grid counterpoise correction.

IV. BENCHMARK APPLICATIONS

We compare the QLDFT method within the two approximations (LIE-0 and LIE-1) for two benchmark systems with classical molecular-dynamics simulations employing the same numerical approximations, that is, featureless-point approximation for the hydrogen molecules, and the same $v_{12}(\mathbf{r})$ interaction potential, same boundary conditions (same simulation boxes, periodic boundary conditions, Γ-point approximation). The first benchmark system is a slit pore with a hard-wall potential, which we use to observe the effects of confinement on adsorption thermodynamics and the fluid

structure. The second test case is hydrogen gas at different temperatures with a fixed hydrogen molecule at the origin, intended to examine the center-of-mass radial distribution function of the uniform fluid.

To approach a fair comparison with classical MD results, we "switch off" quantum effects due to the external potential, by choosing a large value for the particle mass m in Eq. (4) (typically ≈ 250 amu; a finite value is needed to maintain stability of numerical algorithms). Note that a change in the particle mass affects *only* quantum effects due to the external potential. Quantum effects arising from intermolecular interactions are treated implicitly in QLDFT, through the excess functional. These effects are always present, and cannot be switched off. As a result, our comparisons to MD simulations are meaningful only at relatively high temperatures.

A. Adjustable parameters of the LIE-1 functional

We determine r_{cut}, r_0, and d parameters of the LIE-1 functional by fitting density profiles to the results of a classical molecular-dynamics simulation of adsorption in hard-wall slit pores. To remain consistent with the approximations made in QLDFT, the MD simulations were performed for featureless mass points, interacting according to the (uncut) v_{12} spherical part of Diep and Johnson's potential [82].

The CMD trajectories have been pre-equilibrated using Andersen's thermostat with collision rate [91] of 2.5%, decreasing to a value of 10^{-5}, and then adjusted to the target temperature by running a postequilibration over 25 ps, using the Berendsen thermostat [92] with coupling parameter $\tau = 1$ ps. Production trajectories employed the NVE ensemble and were running for several nanoseconds, depending on the particle density, until the density profile was converged. The MD simulations were at $T=150$ K, where quantum effects due to v_{12} interactions are expected to be small [22]. We have chosen slit pores limited by hard walls with pore sizes of 4, 8, and 16 Å, representing typical pore sizes for hydrogen adsorption in various applications. Note that slit pores are only repulsive at the hard walls so that a hard slit pore of 4 Å could be compared roughly with a graphene slit pore at 9 Å interlayer spacing. The average hydrogen density in the pores was 64 kg m^{-3}, representing rather high storage capacities and hence a strong influence of the interparticle potential.

Figure 1 compares the classical MD densities with classical-limit QLDFT densities. The pore sizes are chosen such that the hydrogen fluid density shows qualitative differences in density profiles. In all three cases, the global maximum of the density is at the turning points at the pore walls. For the 4 Å slit pore, only one minimum of the fluid density is observed at the pore center. The 8 Å pore shows two minima and the secondary maximum at the pore center, while the 16 Å pore shows both the pronounced oscillations close to the wall and a smooth density profile in the pore center. Thus, the test set includes a reasonable distribution of pore sizes which are present in nanoporous materials with appreciable hydrogen abundance.

The three adjustable parameters of the LIE-1 functional were chosen to fit the $R=16$ Å density profile. The part of

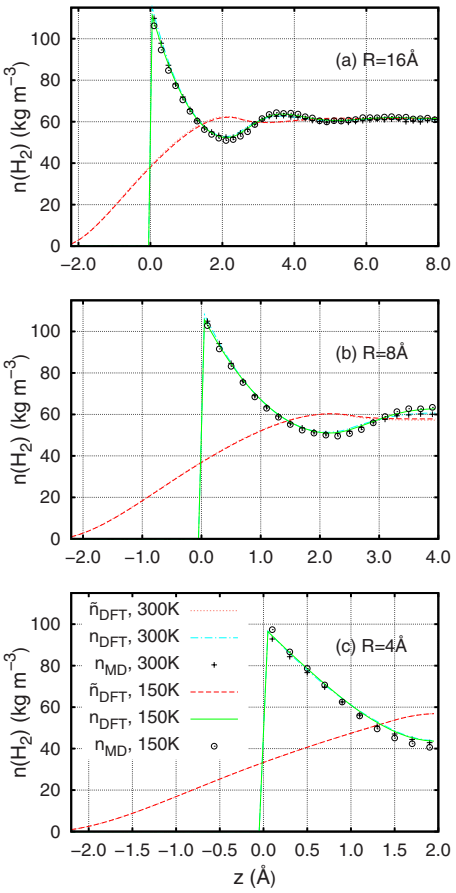

FIG. 1. (Color online) Laterally averaged hydrogen density profiles in hard-wall slit pores: classical molecular-dynamics reference calculations (open circles) are compared to classical limit ($m \to \infty$) of QLDFT within the LIE-1 approximation (solid green lines) for a slit pore of (a) 16, (b) 8, and (c) 4 Å width. The pore wall is at $z=0$, with only the left half of the pore shown in each case. Note that only the 150 K data were used in fitting the LIE-1 adjustable parameters. The weighted density $\bar{n}$ in the same pores are shown for comparison (dashed red line). The finite slope of the QLDFT density profiles at $z=0$ (and $z=R$) is an artifact of the finite grid resolution used in the simulations. Only the $R=16$ Å $T=150$ K MD profiles were used for determining the adjustable parameters of the LIE-1 functional.

the profile in the immediate vicinity of the turning point is specific to the hard-wall potential and is not relevant for the more realistic confining potentials, which would be expected for H_2 storage applications. Therefore, we excluded density points closer than 0.9 Å to the pore wall from the fit.

The classical MD and the LIE-1 QLDFT density profiles are in all three test sets very close. Moreover, the agreement between both simulation techniques remains very similar also for the high-temperature calculation at 300 K, which were not used for fitting the adjustable parameters of the functional.

For comparison, we also show the weighted density $\bar{n}$ in the same pores. As expected, it is much smoother than the physical density n and is essentially temperature independent for a given size of the slit pore. The weighted density also remains nonzero below the barrier as the consequence of the

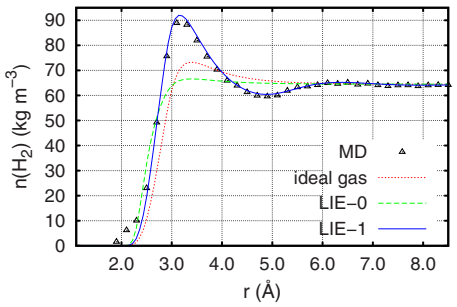

FIG. 2. (Color online) Simulated center of mass radial distribution function for classical uniform hydrogen fluid of average density of 64 kg m^{-3} at $T=300$ K. Triangles are the results of a 20 ps classical MD run in a 25 Å periodic box containing 299 H_2 molecules. Classical ideal gas (dotted red line) and classical ($m\to\infty$) limit of QLDFT within the LIE-0 (dashed green line) and LIE-1 (solid blue line) approximations. Ideal-gas and QLDFT simulations are in a 20 Å periodic box with 0.133 Å grid spacing, with the probe potential $[v_{12}(r)]$ at the center of the box. The shoulder in the MD profile at low r is an artifact of the binning procedure used to construct the profile.

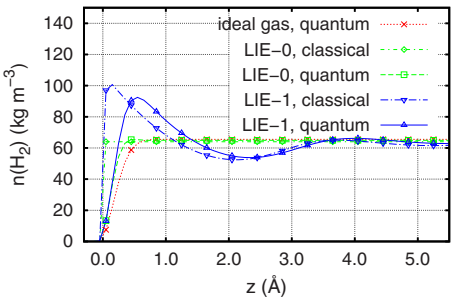

FIG. 3. (Color online) Hydrogen density profiles in a 20 Å hard-wall slit pore at 100 K and 64 kg m^{-3} average H_2 density. Only the left-hand side of the pore is shown, with the pore wall at $z=0$. Density oscillations are not visually discernible beyond $z\geq 5$ Å away from the wall. For the classical profiles (LIE-0: dot-dashed green line; LIE-1: dot-long-dash blue line), the finite rising slope at the wall is an artifact of the finite resolution of the numerical grid. The quantized Boltzmann ideal gas profile (dotted red line) is given by $n(z)\approx n_0[1-\exp(-4\pi z^2/\lambda_D^2)]$, where λ_D is the de Broglie wavelength.

inability of the spherical convolution filter of Eq. (23) to recognize the left/right asymmetry.

B. Radial distribution functions in fluid H_2

As an effective single-particle theory, QLDFT does not give direct access to the radial distribution function (RDF) of the uniform fluid. The standard approach for extracting this information is to perform a nonuniform simulation in the external potential generated by a fluid particle fixed at the coordinate origin. The density profile in this probe potential yields the RDF. The calculated radial density profiles are shown in Fig. 2, in comparison to the classical MD simulation at the same temperature and average density.

The LIE-0 approximation, which does not include any information on the explicit form of the intermolecular potential, yields a completely flat profile for $r\geq 3$ Å. The density goes sharply to zero at shorter distances (dashed green line), leaving a spherical "hole" of $R\approx 2.3$ Å. The oscillations in the LIE-0 density profile are in fact *smaller* than the modulation found in the ideal gas in the same central probe potential (dotted red line). This result is not unexpected: in the absence of explicit interparticle interactions, replacing a particle at the origin with the probe potential should not affect the density away from the origin, as long as the effective Hamiltonian matches the equation of state for the probe v_{12}. Any gain or loss in $v_{ext}=v_{12}$ in this region is effectively compensated by v_{XC}.

Incorporation of explicit effective interparticle interactions in the Hamiltonian through the mean-field and nonlocal v_{XC} terms recovers the correct density profile. Indeed, the calculated classical limit of the LIE-1 density profile (solid blue line) nearly coincides with the MD result. Both MD and LIE-1 distributions show a maximum of the radial distribution at ≈3.1 Å, followed by decreasing oscillations closely matching the typical behavior of a liquid expected for fluid H_2 at this density [93]. Because the LIE-1 density profile in Fig. 2 is obtained with the adjustable parameters determined in a rather different physical environment (hard-wall slit pore), the functional appears to have some degree of transferability.

C. Quantum effects: Hard-wall slit pores at low temperature

All QLDFT results reported to this point were obtained in the classical ($m\to\infty$) limit. We are now ready to discuss the consequences of quantization of the center of mass motion in the external potential. Our first example is a 20-Å hard-wall slit pore, at 100 K and an average H_2 density of 64 kg m^{-3}. Density profiles calculated using LIE-0 and LIE-1 functionals in the classical and quantized limits are shown in Fig. 3. The density profile for the quantized Boltzmann ideal gas is also shown for comparison.

The only feature discernible for the quantized ideal gas is the sharp rise at the wall, with the density reaching 95% of the bulk value at the distance $\approx 0.5\lambda_D$ [$\lambda_D=(2\pi\hbar^2/mkT)^{1/2}$ is the de Broglie wavelength]. An even sharper rise is observed for the local LIE-0 functional (dashed green curve in Fig. 3), reflecting the increased number of interparticle contacts away from the wall. The rest of the quantized LIE-0 profile is however featureless. The initial part of the quantized LIE-1 profile (solid blue line) closely matches LIE-0, up to $z\approx 0.2$ Å. The direct quantum effect—standing wave reflection at the wall—clearly dominates in this area. Unlike LIE-0, quantum effects in the LIE-1 fluid structure persist farther away from the wall: the position of the global maximum of the density shifts away from the wall (classical: $z=0$; quantized: $z\approx 0.57$ Å). The magnitude of the maximum decreases from ≈130 kg m^{-3} (classical) to ≈104 kg m^{-3} (quantized). The positions of the structural minima shift from $z\approx 2.1$ Å (classical) to ≈2.5 Å, while the density at the minimum increases slightly (from ≈49 to ≈51 kg m^{-3}). At this low density and relatively high temperature, the fluid structure become indiscernible beyond $z\geq 5$ Å, both in the classical and quantum limits.

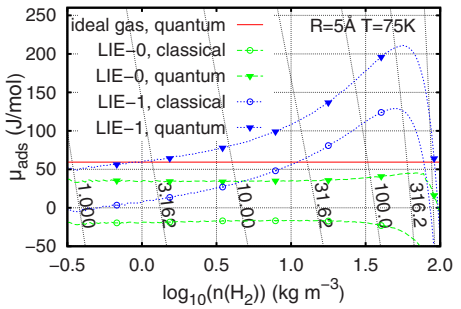

FIG. 4. (Color online) Adsorption free energy for a 5 Å hard-wall slit pore at 75 K. Slanted dotted lines represent the free hydrogen fluid in equilibrium with the adsorbed hydrogen within the pore. Quantity n is the average density of H_2 inside the pore. The sharp decrease in the QLDFT adsorption free energies at very high average densities is due to the local H_2 densities at the walls approaching the freezing line ($\approx$120 kg m^{-3} at 75 K [84]).

In effect, quantum effects create an additional excluded volume close to the repulsive walls. Their effect therefore is to always reduce the available storage capacity [22].

D. Adsorption free energy in a slit pore

Even though the purely local LIE-0 functional is clearly incapable of describing the fluid structure, it nonetheless incorporates direct quantum effects. Our next task is to examine whether LIE-0 can still lead to a reasonable description of these effects in the free energy of adsorption. We calculate adsorption free energies in a 5 Å hard-wall slit pore. The results are shown in Fig. 4.

Even for the quite confined 5 Å pore at 75 K the direct quantum effects are small. The functionals yield direct effects of $\approx$60 J mol^{-1}, with the magnitude of the result remaining nearly constant through the entire density range. The quantum contribution to the adsorption free energy in this system is determined by the change in the fluid structure in the immediate vicinity of the sites exhibiting a rapid change in the adsorption potential (pore wall). Since both LIE-0 and LIE-1 functionals show a nearly identical behavior at the wall, the similar magnitude of the change in the free energy of adsorption is not surprising. Furthermore, since quantized ideal gas shows a very similar density profile immediately at the wall, the corresponding free energy change is also similar.

At the same time, the two functionals show a qualitatively different behavior for the classical packing effects. LIE-0 results (incorrectly) suggest that classical fluid adsorption in this system is slightly favorable. This failure stems from the lack of the explicit v_{12} term in LIE-0 effective Hamiltonian. Although its absence is compensated by the ε_{XC} contribution in the bulk fluid, in the highly inhomogeneous environment of the slit pore LIE-0 credits the system for the attractive interactions to the (nonexistent) H_2 molecules inside pore walls. In contrast, the LIE-1 functional starts at the zero classical adsorption free energy at low coverages and yields steadily increasing value at higher densities. Both functionals give sharply decreasing adsorption free energies at very high densities. In this case, the local densities in the pore approaches H_2 freezing line, taking the functional outside the range of validity of the experimental data used to parametrize $\mathcal{F}$.

V. DISCUSSION

We have developed a quantized fluid DFT scheme for estimation of the free energy of a system of interacting molecules in an external potential. The scheme is based on the Kohn-Sham partitioning of the total energy, commonly used in electronic structure DFT. The practical performance of the technique depends critically on the choice of the excess functional. In this work we explore two general strategies, targeting the functional to the supercritical n-H_2 fluid. The two functional forms are closely related to the approaches which have proven successful in electronic and molecular DFT-the local density and the weighted density approximations.

(i) In the LIE-0 functional, the interparticle interaction is absorbed in the excess functional and does not appear as an individual term in the Hamiltonian. This is motivated by the weak attractive part of the intermolecular interaction in H_2 (less than 80 K). The excess functional in the LDA approximation is then uniquely defined by the experimental equation of state for the normal hydrogen gas. This approximation gives reasonable thermodynamic results for low-pressure hydrogen in slowly varying external potentials, but fails to reproduce the correct fluid structure of liquid hydrogen and thermodynamic properties of narrow-pore adsorption.

(ii) If the explicit interparticle potential is included in the Hamiltonian, direct application of the LDA excess functional often leads to numerical problems due to strong potential oscillations, at least in our 3D real space implementation. This problem is known from the literature, and a well-known solution is the weighted density approximation (WDA) as excess functional [65,66,94]. We refer to the combination of interparticle potential and WDA excess functional as LIE-1.

We have carried out benchmark calculations for hydrogen subject to a H_2 probe potential and confined in a slit pore with hard walls. Both simulations are not subject to additional numerical issues as for example a parametrized host-guest potential. Nonetheless, they offer to study the performance of QLDFT over a large range of physically relevant situations, such as the shape of the liquid structure hydrogen density at a probe potential or at a hard wall, the correct limit of the hydrogen density for the free hydrogen gas, and the role of quantum effects for low temperatures.

We have observed that the hydrogen density profile differs strongly between the LIE-0 and LIE-1 approximations. In the view of the drastic approximations made in the LIE-0 approximation for the mean-field potential and the form of the excess potential, LIE-0 QLDFT should not be expected to reproduce liquid structure, freezing (see [27] for a detailed formal analysis), nucleation, or fluid phase separations. A reasonable description of the density oscillations at solid walls should also not be expected. At the same time, closely related LDA classical-fluid DFT theories give accurate predictions for the average density profiles [95–97] and the adsorption free energies [28,96,98], especially above the bulk critical point [8,41,96,98].

These observations from the literature are reflected in our benchmark calculations. Even though LIE-0 fails to reproduce the correct density profiles, the oscillations of the LIE-1 density around the nearly constant LIE-0 values cancel each other to a large extent. Therefore, for reasonably large pore sizes LIE-0 and LIE-1 will give very similar average densities for any given temperature and pressure, and hence thermodynamical properties in nanoporous structures are reproduced rather well within the LIE-0 approximation, as long as the direct quantum effects dominate.

QLDFT does provide reasonable results for a large range of temperatures (above 100 K) and hydrogen densities even in confined environments such as small slit pores, provided that the Hamiltonian includes the interparticle interaction and the nonlocal effects (e.g., through the weighted density approximation). LIE-1 QLDFT does reproduce the fluid structure, classical packing effects, and the thermodynamic properties. While the featureless particle approximation and neglect of the quantum statistics prevents its application to low-temperature systems, LIE-1 QLDFT application to technologically relevant hydrogen storage applications at and above liquid nitrogen temperature (77 K) are possible with great confidence, provided a reliable external potential (host-H_2) is available.

VI. SUMMARY AND OUTLOOK

We developed a finite-temperature quantized density-functional theory designed to study the adsorption of light molecular and atomic species in nanoporous materials. Quantization of the guest motion in the adsorbing potential is treated through the Kohn-Sham partitioning of the free energy, with contributions due to the noninteracting reference fluid evaluated exactly. The remaining terms are subsumed by an excess functional, parametrized to reproduce experimental equation of state of the free uniform fluid. The treatment is applicable at temperatures well above the quantum condensation limit.

We explore the simplest possible form of the excess functional—the local interaction expression (LIE-0), where all interactions between the fluid particles are assumed to be contact. Even this crude approximation corrects many of the shortcomings of our scaled ideal-gas treatment [63,64]. The more sophisticated LIE-1 treatment includes the H_2-H_2 potential v_{12} and correctly recovers the liquid fluid density oscillations at hard walls and at a probe potential.

Both LIE functionals discussed here permit an efficient numerical implementation on 3D Cartesian product grids. The resulting code is robust and can be applied with minimal manual intervention, allowing studies of large systems and rapid screening of a large variety of potential hydrogen storage candidate systems.

We benchmarked the method on a H_2 probe potential and on slit pores with hard walls. In a forthcoming work [99] we will apply the method to hydrogen adsorption in graphite slit pores, carbon nanotubes, fullerenes, and graphitic carbon inverse opals.

We are currently investigating several potential extensions and improvements of the method. An important issue is the availability of high-quality host-guest potentials. We explore the parametrization of adsorption force fields, describing the interaction of molecular hydrogen and other light guests (He, CH_4) with a large set of elements and chemical environments, present in various nanoporous systems.

Another direction of development relates to an explicit treatment of the internal degrees of freedom of the guest particles. Although the present featureless particle approximation appears to provide a reasonable description of hydrogen molecule in a dispersive environment [64], the situation is likely to change in the presence of strong electric fields. For hydrogen, the most important internal degree of freedom is molecular rotation [100], especially due to the nuclear statistics issues, and slow ortho/parainterconversion at low temperatures. In the presence of $(M-1)$ internal state variables (in addition to the particle density), the quantities n, v_{XC}, v_{eff}, and ρ_S would be given by M-element vectors, while v_{12} would become an $M \times M$ tensor. Then, if multiplications of vectors and tensors in Eqs. (1)–(8) are understood as inner products, the form of all expressions above remains unchanged. Alternative possibilities to go beyond the featureless particle approximation as it has been proposed by Chandler and co-workers [38,101].

The development of a more sophisticated self-interaction corrected nonlocal excess functional might further improve the performance of QLDFT. Various possibilities in this direction have been explored for classical-liquid DFT. The recent work of Lischner and Ariel [38] provides a strategy to construct functionals in a less *ad hoc* way, which we might pursue in the future. For a QLDFT computer code see Ref. [68]

ACKNOWLEDGMENTS

T.H. acknowledges financial support by the German Research Council [Deutsche Forschungsgemeinschaft (DFG)]. S.P. acknowledges partial support by the National Science Foundation under Grant No. PHY05-51164. We thank Benjamin Schrauf (Jacobs University) for the assistance in running the molecular-dynamics reference calculations, and Dr. Lyuben Zhechkov (Jacobs University) for testing the software implementation of the method.

APPENDIX A: CYCLIC-HAMILTONIAN LIMIT FOR THE KINETIC ONE-PARTICLE PARTITION FUNCTION

We would like to determine the converged limit of the partition function Z_{kin} [Eq. (12)] for the kinetic one-particle Hamiltonian [$v_{eff}=0$ in Eq. (4)]. Three-point discretization of the Hamiltonian on a uniformly spaced Cartesian product grid (Sec. III) leads to a six-diagonal cyclic Hamiltonian. The well-known eigenvalues of this Hamiltonian are given by

$$\epsilon(i,j,k) = \epsilon_x(i) + \epsilon_y(j) + \epsilon_z(k), \tag{A1}$$

$$\epsilon_s(i) = \frac{n_s^2}{ml_s^2}\left[1 - \cos\left(\frac{2\pi i}{n_s}\right)\right], \tag{A2}$$

where l_s is the extent of the simulation box in the s direction ($s=x,y,z$), n_x is the number of grid points along this direc-

TABLE I. Expansion coefficients of the experimental equation of state of n-H_2 [Eq. (B1)]. Values from Ref. [84] are converted to the SI units.

P^a	T^b	$V_{a,b}$
P^{-1}	1	-9.1077×10^{2}
$P^{-2/3}$	1	-3.7326
$P^{-1/3}$	1	1.7117×10^{-2}
P^{-1}	T^{-1}	-3.1811×10^{3}
P^{-1}	$T^{-1/2}$	7.0150×10^{3}
$P^{-1/3}$	$T^{-1/2}$	-1.0480×10^{-2}
P^{-1}	T^{1}	1.1147×10^{1}
$P^{-2/3}$	T^{1}	-4.6496×10^{-3}
$P^{-1/3}$	T^{1}	1.5386×10^{-6}

tion, and i,j,k take values from 0 to n_s-1. The partition function is then given by

$$Z_{kin} = Z_{kin,x}Z_{kin,y}Z_{kin,z}, \tag{A3}$$

$$Z_{kin,s} = \sum_{i=0}^{n_s-1} \exp[-\beta\epsilon_s(i)], \tag{A4}$$

where $s=x,y,z$. Expanding ϵ_s through the second order in i and taking the limit $n_s\to\infty$, we obtain

$$Z_{kin,s} = \theta_3\left[0,\exp\left(-\frac{2\pi^2\beta}{ml_s^2}\right)\right], \tag{A5}$$

where θ_3 is the elliptic theta function of the third kind [102]. Finally, series expansion of the θ_3 function [102] leads to a rapidly converging infinite sum

$$Z_{kin,s} = 1 + 2\sum_{i=1}^{\infty}(-1)^i\left[\exp\left(-\frac{2\pi^2\beta}{ml_s^2}\right)\right]^{i^2}. \tag{A6}$$

At sufficiently high temperatures, the kinetic partition function calculated from Eqs. (A3) and (A6) agrees closely with the continuous limit [Eq. (13)]. A significant difference between the two results indicates the onset of degeneracy of the ideal Boltzmann gas, where our choice of the noninteracting reference ensemble is no longer appropriate.

APPENDIX B: FREE ENERGY OF THE HOMOGENEOUS n-H_2 GAS

Evaluation of the excess energy density ε_{XC} [Eq. (14)] and the excess potential v_{XC} [Eq. (10)] requires free energy of the hydrogen fluid in a wide range of densities and temperatures. We derive the closed-form expression for the free energies from the experimental equation of state of n-H_2 reported by Mills *et al.* [84]:

$$V(T,P) = \sum_{a,b} V_{a,b}P^aT^b, \tag{B1}$$

where T is temperature in K, P is pressure in Pa, and V is molar volume in $m^3\ mol^{-1}$. The coefficients $C_{a,b}$ are collected in Table I. The equation of state is applicable for $2<P<20$ kbar and $75<T<307$ K, as long as the temperature remains above the hydrogen freezing line [84]. The normal hydrogen heat capacity at $P=2$ kbar is given by [84]

TABLE II. Expansion coefficients for isobaric heat capacity of n-H_2 at 1 kbar [Eq. (B2)]. Values from Ref. [84] are converted to the SI units.

T^b	C_b
1	1.2593×10^{3}
T^{-1}	3.1638×10^{4}
$T^{-1/2}$	-1.0512×10^{4}
$T^{1/2}$	-6.1468×10^{1}
T^{1}	1.1230

$$C_p(T,2\ \text{kbar}) = \sum_b C_bT^b. \tag{B2}$$

The coefficients C_b are collected in Table II. Additionally, we require two parameters to fix the (arbitrary) reference state. We choose entropy and Gibbs free energy at 300 K and 1 kbar [85]:

$$S(300\ \text{K},1\ \text{kbar}) = 84.24\ \text{J/K mol}, \tag{B3}$$

$$G(300\ \text{K},1\ \text{kbar}) = -15.397\ \text{kJ/mol}. \tag{B4}$$

The standard approach (see, e.g., [78]) for the construction of the Helmholtz free energy would have been to use the relation:

TABLE III. Expansion coefficients for the free energy $\mathcal{F}$ of n-H_2 [Eq. (B11)].

$f_a(P)$	$g_b(T)$	$F_{a,b}$
1	T^{-1}	6.4026×10^{4}
1	$T^{-1/2}$	-1.3577×10^{5}
1	1	2.7400×10^{4}
1	$\log T$	3.1640×10^{4}
1	$T^{1/2}$	-4.2048×10^{4}
1	T	7.4630×10^{3}
1	$T\log T$	-1.2593×10^{3}
1	$T^{3/2}$	8.1957×10^{1}
1	T^{2}	-5.6150×10^{-1}
$\log P$	$T^{-1/2}$	7.0150×10^{3}
$\log P$	T^{-1}	-3.1811×10^{3}
$\log P$	1	-9.1077×10^{2}
$\log P$	T	1.1147×10^{1}
$P^{1/3}$	1	-7.4653
$P^{1/3}$	T	-9.2992×10^{-3}
$P^{2/3}$	$T^{-1/2}$	-5.2399×10^{-3}
$P^{2/3}$	1	8.5585×10^{-3}
$P^{2/3}$	T	7.6930×10^{-7}

$$F(T,V) = F(T,V_0) - \int_{V_0}^{V} P(T,V')dV'.$$

Inversion of the experimental $V(T,P)$ [Eq. (B1)] leads to cubic radicals, and the form of the resulting expression for $F(T,V)$ is unwieldy. Instead, we choose a more round-about but equivalent way and construct $F(T,P)$:

$$C_p(T,P) = C_p(T,2\ \text{kbar}) - T\int_{2\ \text{kbar}}^{P}\left(\frac{\partial^2 V}{\partial T^2}\right)_p dP, \quad \text{(B5)}$$

$$S(300\ \text{K},P) = S(300\ \text{K},1\ \text{kbar}) - \int_{1\ \text{kbar}}^{P}\left(\frac{\partial V}{\partial T}\right)_p dP, \quad \text{(B6)}$$

$$S(T,P) = S(300\ \text{K},P) + \int_{300\ \text{K}}^{T}\frac{C_p}{T}dT, \quad \text{(B7)}$$

$$G(300,P) = G(300\ \text{K},1\ \text{kbar}) + \int_{1\ \text{kbar}}^{P} VdP, \quad \text{(B8)}$$

$$G(T,P) = G(300\ \text{K},P) - \int_{300\ \text{K}}^{T} SdT, \quad \text{(B9)}$$

$$F(T,P) = G(T,P) - PV. \quad \text{(B10)}$$

The final result for $\mathcal{F}$ is given by

$$\mathcal{F}(T,P) = \sum_{a,b} F_{a,b} f_a(P) g_b(T), \quad \text{(B11)}$$

where T is in K, P is in Pa, and $\mathcal{F}$ is obtained in J mol^{-1}. Coefficients $F_{a,b}$ are collected in Table III. Comparison to tabulated data [85] suggests that extrapolation of the equation of state and the free energy to lower pressures agrees to within 10% of the experimental data for pressures down to 1 bar and behaves sensibly for pressures between 10^{-3} and 10^{12} Pa.

[1] V. I. Kalikmanov, *Statistical Physics of Fluids: Basic Concepts and Applications* (Springer, Berlin, 2001).
[2] A. V. Neimark, P. I. Ravikovitch, and A. Vishnyakov, J. Phys.: Condens. Matter **15**, 347 (2003).
[3] J. Wu, AIChE J. **52**, 1169 (2006).
[4] C. Alba-Simionesco, B. Coasne, G. Dosseh, G. Dudziak, K. E. Gubbins, R. Radhakrishnan, and M. Sliwinska-Bartkowiak, J. Phys.: Condens. Matter **18**, R15 (2006).
[5] M. Eddaoudi, J. Kim, N. Rosi, D. Vodak, J. Wachter, M. O'Keeffe, and O. M. Yaghi, Science **295**, 469 (2002).
[6] J. Jagiello and M. Thommes, Carbon **42**, 1227 (2004).
[7] M. B. Sweatman and N. Quirke, J. Phys. Chem. B **109**, 10381 (2005).
[8] M. B. Sweatman and N. Quirke, Mol. Simul. **31**, 667 (2005).
[9] A. Kuc, L. Zhechkov, S. Patchkovskii, G. Seifert, and T. Heine, Nano Lett. **7**, 1 (2007).
[10] Q. Wang, S. R. Challa, D. S. Sholl, and J. K. Johnson, Phys. Rev. Lett. **82**, 956 (1999).
[11] A. V. Anil Kumar and S. K. Bhatia, Phys. Rev. Lett. **95**, 245901 (2005).
[12] K. M. Thomas, Catal. Today **120**, 389 (2007).
[13] *IPCC Fourth Assessment Report* (UNEP Intergovernmental Panel On Climate Change, http://www.ipcc.ch/ipccreports/ar4-syr.htm, 2007).
[14] J. Kern, *HYCAR* (http://www.hycar.de, 2007).
[15] *Roads2HyCom Communities Handbook Volume A* (European Commission, http://www.roads2hy.com/Downloads/Roads2HyCom%20Communities%20Handbook%20Vol%20A.pdf, 2007).
[16] M. Becher, M. Haluska, M. Hirscher, A. Quintel, V. Skakalova, U. Dettlaff-Weglikovska, X. Chen, M. Hulman, Y. Choi, S. Roth *et al.*, C. R. Phys. **4**, 1055 (2003).
[17] M. Hirscher and B. Panella, Scr. Mater. **56**, 809 (2007).
[18] D. L. Valladares, R. Reinoso, and G. Zgrablich, Carbon **36**, 1491 (1998).
[19] D. Frenkel and B. Smit, *Understanding Molecular Simulations: From Algorithms to Applications* (Academic Press, San Diego, 2002).
[20] G. Garberoglio, A. I. Skoulidas, and J. K. Johnson, J. Phys. Chem. B **109**, 13094 (2005).
[21] A. V. A. Kumar, H. Jobic, and S. K. Bhatia, J. Phys. Chem. B **110**, 16666 (2006).
[22] Q. Wang, J. K. Johnson, and J. Q. Broughton, J. Chem. Phys. **107**, 5108 (1997).
[23] P. Kowalczyk, H. Tanaka, R. Hołyst, K. Kaneko, T. Ohmori, and J. Miyamoto, J. Phys. Chem. B **109**, 17174 (2005).
[24] W. F. Saam and C. Ebner, Phys. Rev. A **15**, 2566 (1977).
[25] R. Evans, Adv. Phys. **28**, 143 (1979).
[26] Y. Singh, Phys. Rep. **207**, 351 (1991).
[27] M. Sweatman, Mol. Phys. **98**, 573 (2000).
[28] M. Schmidt, J. Phys.: Condens. Matter **15**, S101 (2003).
[29] M. B. Sweatman, Phys. Rev. E **77**, 026712 (2008).
[30] Y. Drossinos and P. G. Kevrekidis, Phys. Rev. E **67**, 026127 (2003).
[31] D. Reguera and H. Reiss, J. Chem. Phys. **120**, 2558 (2004).
[32] D. di Caprio and J. Stafiej, J. Mol. Liq. **131-132**, 48 (2007).
[33] E. Ruckenstein and Y. S. Dyikaev, Adv. Colloid Interface Sci. **118**, 51 (2005).
[34] G. S. Heffelfinger, Z. Tan, K. E. Gubbins, U. M. B. Marconi, and F. van Swol, Mol. Simul. **2**, 393 (1989).
[35] E. Kierlik and M. L. Rosinberg, Phys. Rev. A **44**, 5025 (1991).
[36] P. Tarazona and R. Evans, Mol. Phys. **52**, 847 (1984).
[37] K. Jaqaman, K. Tuncay, and P. J. Ortoleva, J. Chem. Phys. **120**, 926 (2004).
[38] J. Lischner and T. A. Arias, Phys. Rev. Lett. **101**, 216401 (2008).
[39] H. Löwen, Phys. Rep. **237**, 249 (1994).
[40] M. Oettel, Phys. Rev. E **69**, 041404 (2004).
[41] R. Evans and U. M. B. Marconi, J. Chem. Soc., Faraday Trans. **82**, 1763 (1986).

[42] P. I. Ravikovitch, A. Vishnyakov, and A. V. Neimark, Phys. Rev. E **64**, 011602 (2001).
[43] L. J. Douglas Frink and A. G. Salinger, J. Comput. Phys. **159**, 407 (2000).
[44] Y. Rosenfeld, M. Schmidt, H. Löwen, and P. Tarazona, Phys. Rev. E **55**, 4245 (1997).
[45] P. Tarazona, Phys. Rev. Lett. **84**, 694 (2000).
[46] M. Schmidt, Phys. Rev. E **60**, R6291 (1999).
[47] M. B. Sweatman and N. Quirke, J. Phys. Chem. B **109**, 10389 (2005).
[48] W. Kohn and L. J. Sham, Phys. Rev. **140**, A1133 (1965).
[49] N. D. Mermin, Phys. Rev. **137**, A1441 (1965).
[50] S. Stringari and J. Treiner, Phys. Rev. B **36**, 8369 (1987).
[51] G. Senatore and G. Pastore, Phys. Rev. Lett. **64**, 303 (1990).
[52] J. Dupont-Roc, M. Himbert, N. Pavloff, and J. Treiner, J. Low Temp. Phys. **81**, 31 (1990).
[53] A. R. Denton, P. Nielaba, K. J. Runge, and N. W. Ashcroft, J. Phys.: Condens. Matter **3**, 593 (1991).
[54] F. Dalfovo, Z. Phys. D: At., Mol. Clusters **29**, 61 (1994).
[55] T. Nakatsukasa, K. Yabana, and G. F. Bertsch, Phys. Rev. A **65**, 032512 (2002).
[56] J. Mur-Petit, A. Sarsa, J. Navarro, and A. Polls, Phys. Rev. B **72**, 104513 (2005).
[57] C. Ebner and W. F. Saam, Phys. Rev. B **12**, 923 (1975).
[58] J. D. McCoy, S. W. Rick, and A. D. J. Haymet, J. Chem. Phys. **92**, 3034 (1990).
[59] S. W. Rick, J. D. McCoy, and A. D. J. Haymet, J. Chem. Phys. **92**, 3040 (1990).
[60] M. A. Hooper and S. Nordholm, Aust. J. Chem. **33**, 2029 (1980).
[61] M. A. Hooper and S. Nordholm, Mol. Phys. **47**, 329 (1982).
[62] T. Biben and D. Frenkel, J. Phys.: Condens. Matter **14**, 9077 (2002).
[63] S. Patchkovskii, J. S. Tse, S. N. Yurchenko, T. Heine, L. Zhechkov, and G. Seifert, Proc. Natl. Acad. Sci. U.S.A. **102**, 10439 (2005).
[64] S. Patchkovskii and T. Heine, Phys. Chem. Chem. Phys. **9**, 2697 (2007).
[65] W. A. Curtin and N. W. Ashcroft, Phys. Rev. A **32**, 2909 (1985).
[66] S. Moroni and G. Senatore, Phys. Rev. B **44**, 9864 (1991).
[67] GNU General Public License, *Version 3* (Free Software Foundation, http://www.fsf.org/licensing/licenses/gpl.html, 2007).
[68] See EPAPS Document No. E-PLEEE8-80-216908 for Fortran-90 computer source code, implementing LIE-0 and LIE-1 QLDFT equations. The code is provided under the terms of GNU General Public License, Version 3 [67]. For more information on EPAPS, see http://www.aip.org/pubservs/epaps.html.
[69] D. J. Lee, M. M. Telo da Gama, and K. E. Gubbins, J. Chem. Phys. **85**, 490 (1986).
[70] R. P. Feynman, *Statistical Mechanics: A Set of Lectures* (Perseus Books, Reading, Massachusetts, 1972).
[71] M. Levy, Phys. Rev. A **26**, 1200 (1982).
[72] P. Hohenberg and W. Kohn, Phys. Rev. **136**, B864 (1964).
[73] R. G. Parr and W. Yang, *Density-Functional Theory of Atoms and Molecules* (Oxford University Press, New York, 1994).
[74] W. Greiner, L. Neise, and H. Stöcker, *Thermodynamics and Statistical Mechanics* (Springer, New York, 2004).
[75] K. Shinoda, S. Miura, and S. Okazaki, J. Chem. Phys. **115**, 4161 (2001).
[76] S. N. Yurchenko, S. Patchkovskii, and T. Heine (unpublished).
[77] J. P. Perdew, R. G. Parr, M. Levy, and J. L. Balduz, Jr., Phys. Rev. Lett. **49**, 1691 (1982).
[78] D. Reguera, R. K. Bowles, Y. Djikaev, and H. Reiss, J. Chem. Phys. **118**, 340 (2003).
[79] J. A. Hernando and L. Blum, J. Phys.: Condens. Matter **13**, L577 (2001).
[80] J. A. Hernando, J. Phys.: Condens. Matter **14**, 303 (2002).
[81] S. F. Boys and F. Bernardi, Mol. Phys. **19**, 553 (1970).
[82] P. Diep and J. K. Johnson, J. Chem. Phys. **112**, 4465 (2000).
[83] J. D. Weeks, D. Chandler, and H. C. Andersen, J. Chem. Phys. **54**, 5237 (1971).
[84] R. L. Mills, D. H. Liebenberg, J. C. Bronson, and L. C. Schmidt, J. Chem. Phys. **66**, 3076 (1977).
[85] R. McCarty, J. Hord, and H. Roder, *Selected Properties of Hydrogen (Engineering Design Data): U.S. NBS Monograph 168* (U.S. National Bureau of Standards, Washington, D.C., 1981).
[86] A. González, J. A. White, F. L. Román, S. Velasco, and R. Evans, Phys. Rev. Lett. **79**, 2466 (1997).
[87] A. González, J. A. White, F. L. Román, and R. Evans, J. Chem. Phys. **109**, 3637 (1998).
[88] Y. Rosenfeld, Phys. Rev. Lett. **63**, 980 (1989).
[89] R. M. Wilcox, J. Math. Phys. **8**, 962 (1967).
[90] D. Prato and C. Tsallis, J. Math. Phys. **41**, 3278 (2000).
[91] H. C. Andersen, J. Chem. Phys. **72**, 2384 (1980).
[92] H. J. C. Berendsen, J. P. M. Postma, W. F. van Gunsteren, A. DiNola, and J. R. Haak, J. Chem. Phys. **81**, 3684 (1984).
[93] M. P. Allen and D. J. Tildesley, *Computer Simulation of Liquids* (Oxford University Press, Oxford, 1989).
[94] N. Ashcroft, Aust. J. Phys. **49**, 3 (1996).
[95] J. P. R. B. Walton and N. Quirke, Chem. Phys. Lett. **129**, 382 (1986).
[96] P. Tarazona, Mol. Phys. **60**, 573 (1987).
[97] J. G. Powles, G. Rickayzen, and M. L. Williams, Mol. Phys. **64**, 33 (1988).
[98] Z. Tan and K. E. Gubbins, J. Phys. Chem. **94**, 6061 (1990).
[99] S. Patchkovskii and T. Heine (unpublished).
[100] B. C. Hathorn, B. G. Sumpter, and D. W. Noid, Phys. Rev. A **64**, 022903 (2001).
[101] D. Chandler, J. D. McCoy, and S. J. Singer, J. Chem. Phys. **85**, 5971 (1986).
[102] *Handbook of Mathematical Functions*, edited by M. Abramowitz and I. A. Stegun (Dover Publications, New York, 1972).